Bifurcation Analysis of Active Electrical Distribution Networks Considering Load Tap Changers and Power Converter Capacity Limits

Dionysios Moutevelis, Javier Roldán-Pérez, *Member, IEEE*, Milan Prodanovic, *Member, IEEE*, and Santiago Sanchez-Acevedo, *Member, IEEE*

***Abstract*—The aim of this article is to analyze the parameter stability and power transfer limits of active distribution networks with power converters and load tap changers by using bifurcation theory. First, the nonlinear model of a representative distribution grid with mixed loads and power converters is derived. Frequently neglected effects of converter capacity limits and transformers with load tap changers are considered, and for this purpose, static and dynamic saturations are modeled by using approximations based on smooth functions. In addition, a solution based on an antiwindup scheme is provided to model load tap changers without numerical convergence problems. These methods allow their integration to the model in a comprehensive way. Results show the impact of converter parameters and its limits on system stability as well as the impact of weak grid conditions. Moreover, they show that these effects can destabilize the system under, seemingly, safe operating conditions. The results indicate that reactive power support from converters can improve stability margins and the performed analysis can help in the design of the converter control parameters. Experimental results obtained from the laboratory environment comprising two distributed generators and a grid emulator are used for the validation of the contributions of this article.**

***Index Terms*—Bifurcation theory, electrical distribution systems, nonlinear analysis, reactive power support.**

I. Introduction

STABILITY of an electrical power network has been continuously studied in the past few decades [1]. However, with the recent integration of distributed generation, microgrids, and electric vehicles, the interest in this topic has increased [2]–[4]. A common characteristic of these new grids is the massive presence of converter-interfaced generators and loads. Therefore, the contribution of these elements to the system stability has been singled out as a principal research challenge. Small-signal stability techniques are commonly used to predict dynamic instabilities in these grid scenarios [5]. However, in these techniques, it is assumed that the system variables do not deviate significantly from their nominal operating values. For this reason, nonlinear techniques are preferred in order to study power transfer limits [6], [7]. In particular, bifurcation theory is a technique that is commonly applied to study stability boundaries of nonlinear systems, especially when there is a significant change of system parameters or variables [8], [9]. Bifurcation theory has been used in the past to study voltage collapse in conventional power systems [10]–[12], as well as to study nonlinear phenomena in dc–dc converters, such as buck [13], boost [14], and Cuk [15].

Recently, the research focus has been set on the application of bifurcation theory to the study of dc–ac converters in hybrid networks [16]. For example, Lenz *et al.* [17]–[19] have studied the stability limits of islanded droop-controlled ac and dc microgrids. The scheduling of the droop characteristics for frequency and voltage regulation by using bifurcation theory was suggested in [20]. The impact of constant impedance, constant current, and constant power (ZIP) loads and virtual synchronous machines on the microgrid stability has also been studied by Shuai *et al.* [21], [22]. In these works, it has been shown that bifurcation theory is a powerful tool for assessing the impact of physical parameters on the system stability (e.g., line impedances), as well as for selecting control parameters. Furthermore, it has been demonstrated that this method provides qualitative and quantitative information regarding the resulting instabilities that cannot be identified by using static or small-signal analysis [19].

Bifurcation theory has also been used in conventional power systems in order to find interactions with converter-interfaced applications. For example, the nonlinear effects introduced by wind farms in high-power grids were studied in [23] and [24]. In [25], the same approach was used to study a continuous-time averaged model of a modular multilevel converter connected to a grid. In [26] and [27], bifurcation phenomena were identified in the ac and dc sides of grid-connected converters by using an analytic approach. Despite the fact that there are many publications exploring specific converter applications, grid-connected microgrids and electrical distribution systems received less attention.

Manuscript received July 30, 2021; revised November 4, 2021; accepted December 27, 2021. Date of publication January 7, 2022; date of current version February 18, 2022. This work was supported in part by the European Regional Development Funds, in part by the Community of Madrid Through the Research Project PROMINT-CM under Grant P2018/EMT4366, and in part by the Spanish Government through the Juan de la Cierva Incorporación Program under Grant IJC2019-042342-I. Recommended for publication by Associate Editor F. Wang. *(Corresponding author: Dionysios Moutevelis.)*

Dionysios Moutevelis, Javier Roldán-Pérez, and Milan Prodanovic are with Electrical Systems Unit, IMDEA Energy Institute, 28935 Madrid, Spain (e-mail: dionysios.moutevelis@imdea.org; javier.roldan@imdea.org; milan.prodanovic@imdea.org).

Santiago Sanchez-Acevedo is with SINTEF Energy Research, 7034 Trondheim, Norway (e-mail: santiago.sanchez@sintef.no).

Color versions of one or more figures in this article are available at https://doi.org/10.1109/TPEL.2022.3141234.

Digital Object Identifier 10.1109/TPEL.2022.3141234

In addition, as these works focused on the converter modeling, most of them did not take into account the grid integration aspects, such as the effect of load tap changers (LTCs) and power converter current limits [28].

It has been widely known that LTCs improve voltage stability in electrical distribution systems [7], [29]. Moreover, several works have reported that LTCs can be used to improve the power transfer limits [30]. However, LTCs and other grid elements (such as electronic interfaces) may lead to undesired dynamic interactions, if they are not properly coordinated [31]. Therefore, some authors have suggested that LTCs and other network elements should be coordinated by grid operators [32]. Converter capacity limits also play an important role in the grid stability [33]. In bifurcation stability analysis, they have been considered in recent studies [24], [34], [35]. In [34], capacity limits of power converters were identified as a limiting factor for the stability of a whole distribution system. Therefore, some important mismatches between theoretical and real network results may occur if these limits are not taken into account. More specifically, in [35], a new type of instability resulting from limiting the converter current was reported. However, only static current limits were considered. The modeling of the saturation was achieved by using state variable switching, when the limit was encountered. In [24], a piecewise smooth representation of the system was also considered in order to model the saturation limits. State variable and equation switching is a realistic approach and produces accurate results. However, this methodology increases the problem complexity, and therefore, its application to larger systems may not be straightforward. With this respect, it is of interest to find alternative methods to model LTCs and converter current limiting without increasing the computational burden. Smooth functions have been used in the past to approximate switching phenomena, for example, for the modeling of the diode operation using an exponential function [36]. In the field of power systems, the hyperbolic tangent function has been used in the past to approximate the limits applied in synchronous generator control loops, namely, excitation and turbine speed governor controls [37], [38]. However, its use for the modeling of LTCs and converter current limiting has not been explored. Finally, it is worth mentioning that experimental validation is rarely found in bifurcation studies for multiconverter systems [18], [22]. Therefore, validation of theoretical developments in a laboratory environment is of particular interest.

In this article, stability boundaries of converter-dominated electrical distribution systems are investigated by using bifurcation theory. The full dynamic model of the system is derived, and parametric continuation is implemented by using a MATLAB toolbox called *Matcont* [39]. The analysis considers all the nonlinear effects the converter controllers introduce to the system. This allows a proper assessment of the system operation, even when large deviations from the nominal parameters occur. Results that cannot be derived by linearization, such as limit cycle magnitudes or 2-D stability boundaries, are provided. Compared with other published works, transformer LTCs and converter capacity limits are taken into consideration by using smooth mathematical functions so that the problem complexity does not increase. The conventional dynamic current saturation strategy (commonly used in industrial converters) is modeled. Finally, the contribution of converters to the power system stability via reactive power support is thoroughly investigated. It is shown that capacity limits of electrical distribution systems can be improved by adequately tuning the control parameters of electronic interfaces and bifurcation theory is a useful tool for the selection of their values. All the theoretical developments were tested in the laboratory test bench based on two 15-kVA voltage-source converters (VSCs) connected to a 75-kVA grid emulator.

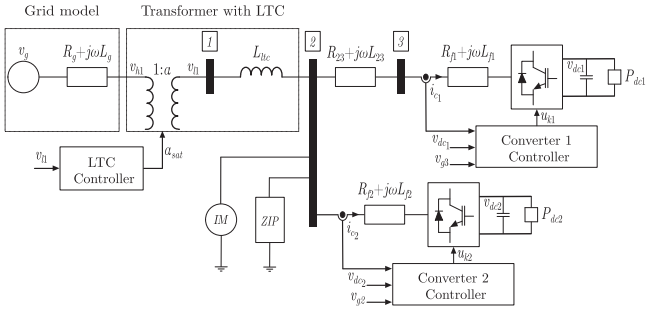

Fig. 1. Diagram of the electrical distribution system studied in this article.

II. System Overview

A. Description of the Electrical Distribution System

Fig. 1 shows the electrical diagram of the distribution network studied in this article. It contains two electronically interfaced loads, a ZIP load, and an induction motor (IM). The electronic interfaces can be used to represent the basic features of distributed generators by reversing the power flow direction. The combination of these three elements represents most load types that can be found in low-voltage electrical distribution networks. The radial topology of the grid and the high R/X ratio chosen for electrical lines are in accordance with the typical characteristics of low-voltage networks [40], [41]. All the elements are connected to a weak grid through a step-down transformer equipped with an LTC device. The main task of this device is to regulate the voltage of Node 1. The grid elements and important modeling procedures are presented in Section III, while the rest of modeling equations are included in the Appendix so that this article is self-contained.

B. VSC Control System

Fig. 2 shows the control system of the VSCs. It consists of two standard ac-current controllers, for direct and quadrature axes, and two outer control loops. The first outer controller calculates the d-axis current reference in order to maintain the dc voltage constant. The other one calculates the q-axis current reference and offers reactive power support during voltage drops. This is achieved by using a droop characteristic that demands or delivers the necessary reactive power when a voltage deviation is measured at the connection point. The bandwidth of these controllers is significantly smaller than that of inner controllers

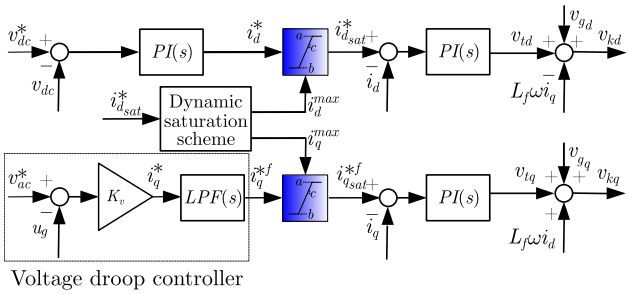

Fig. 2. VSC control system including reactive power droop and dynamic current saturation.

in order to avoid interactions between the loops [42]. The dq current reference is saturated according to the maximum current capacity of the converter. First, the d-axis current is limited to be within the maximum allowed current ($I_{\max}$), while the q-axis current is saturated according to the remaining converter capacity. More information is provided in Section III.

C. Bifurcation Theory Background

Bifurcation theory is a mathematical tool that can be used to study nonlinear dynamic systems. It deals with the emergence of sudden changes in the system response arising from smooth continuous parameter variations [43]. These variations are assumed to occur "slowly," while the system equilibrium is preserved. This assumption is also known as quasi-static assumption [44]. One should note that this assumption, in the general case, does not cover sudden large transients. In order for bifurcation theory to be used in transient or fault studies, specific criteria have to be met, e.g., transient voltage change being equivalent to continuous change [27]. The points where sudden changes emerge are called bifurcation points (BPs).

Power systems can generally be modeled as a set of differential–algebraic equations [1]

$$\begin{aligned}\frac{dx}{dt} &= \dot{x} = f(x, y, p)\\ 0 &= g(x, y, p)\end{aligned} \tag{1}$$

where x is the set of state variables, y is the set of algebraic variables, and p is the set of parameters. The "dot" notation will henceforth signify "time derivative" for brevity. In (1), the variable change $y = G(x, p)$ can always be achieved and $\lambda \in p$ can be selected as the only varying parameter [6], [45]. Then, the system can be transformed in a set of ordinary differential equations:

$$\dot{x} = f(x, G(x, \lambda), \lambda) = F(x, \lambda). \tag{2}$$

For all the values of λ, the equilibrium points of (2) are given by the solution of

$$F(x^*, \lambda) = 0. \tag{3}$$

For each solution, the state matrix can also be defined as

$$A = \left.\frac{\partial F}{\partial x}\right|_{x=x^*}. \tag{4}$$

Saddle-node bifurcation (SNB) and Hopf bifurcation (HB) are the two most common ways in which the stability of the equilibrium point is lost in power systems [46]. The first one is related to monotonic instability and introduces a real eigenvalue in matrix A crossing the imaginary axis. The second one is related to oscillatory instability and leads to a set of complex eigenvalues of A crossing the imaginary axis.

In this article, bifurcation analysis is carried out by using *Matcont*, a MATLAB toolbox. While maintaining equilibrium, it uses test functions to check necessary conditions for the existence of these BPs.

D. Rotating Reference Frames

All the system equations will be analyzed in a common reference frame (DQ) that is synchronized with the ideal grid voltage. However, converter equations for the ith converter are expressed in the local reference frame ($dq - i$) that is generated by their own phase-locked loop (PLL). Complex representations in a synchronous reference frame (SRF) are expressed as $f_{dq} = f_{d-i} + jf_{q-i}$. Transformation of signals (voltages and currents) from the local reference frame to the common reference frame is achieved by using a rotation matrix

$$\begin{bmatrix} f_D \\ f_Q \end{bmatrix} = \begin{bmatrix} \cos\delta_i & -\sin\delta_i \\ \sin\delta_i & \cos\delta_i \end{bmatrix} \begin{bmatrix} f_{d-i} \\ f_{q-i} \end{bmatrix} \tag{5}$$

where δ_i is the angle between the reference frames. More details can be found in the literature [5], [47], [48].

III. Modeling of LTCs and Converter Capacity Limits

This section explains a method to model the dynamic saturation on LTC and VSCs. The rest of the network elements are briefly described (the details can be found in the Appendix).

A. Dynamic Saturation Modeling

In this article, saturation is approximated by using a hyperbolic tangent function [49]

$$x_{\text{sat}} = \frac{1}{2}[(a + b) + (b - a)\tanh(c(x - x_0))] \tag{6}$$

where x and x_{sat} represent the input and saturated output quantities, respectively, while a and b are the minimum and maximum values of the output signal, respectively. These limits could either be constant or adjusted dynamically. Parameter c represents the slope of the tangent function and x_0 is the inflection point of the curve, i.e., the point where the curvature changes sign.

Equation (6) can be simplified if the limits are symmetrical around zero. In this case, $a = -b$ and $x_0 = 0$. To simplify the tuning of the tangent slope and to make the saturator adaptive, the slope is set to $c = 1/b$. Then, (6) can be written as

$$x_{\text{sat}} = b\tanh(x/b). \tag{7}$$

Other methods to adjust the approximation can be used. However, it will be shown that the method described in this article provides adequate results with a reduced number of parameters.

From a theoretical point of view, this modeling method introduces the following advantages.

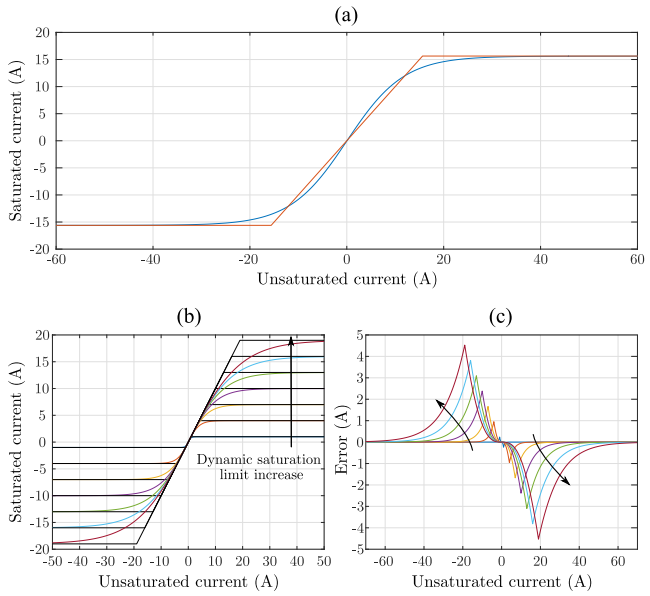

Fig. 3. (a) Approximation of an ideal saturation with a hyperbolic tangent function. (b) Performance of the hyperbolic tangent function when saturation limits are adjusted dynamically. (c) Error between hyperbolic tangent function and ideal saturation with dynamic limits.

1) The whole system is modeled with a set of smooth ordinary differential equations. This overcomes the nonsmooth character of explicit saturation functions. Furthermore, it makes the model compatible with software that supports differential–algebraic systems as well as purely differential ones, e.g., *Matcont* [39]. This modeling method is also compatible with both discrete- and continuous-time solvers.
2) The order of the system is kept constant, and state variables are not switched when limits are encountered. Thus, piecewise functions and complex control procedures are avoided.
3) Numerical problems, such as the integrator windup as well as the trajectory deadlock, are avoided [50]–[52]. Thus, numerical convergence is achieved with minimal reduction of accuracy.
4) No back calculation branches for the current proportional–integral (PI) controllers are necessary. Thus, less time is required for the gain tuning, and the system design process becomes simpler.

Fig. 3(a) illustrates how the proposed function approximates a saturation. Fig. 3(b) illustrates the adaptive character of (7), where the saturation limits have been adjusted according to the input parameters. Fig. 3(c) shows that there are differences between the ideal saturator and the approximation, especially in the corners. The ability to model dynamic saturation phenomena using the adaptive slope of (7) is the tradeoff for the increase of the error near the saturation "knee." In this article, it will be shown that the results are adequate even in the presence of these mismatches around the corners. The use of hyperbolic tangents simplifies the resolution of the differential equations because there are neither sharp variations in the trajectories nor piecewise functions.

B. VSC Modeling

The dc voltage controller can be modeled as follows:

$$\begin{aligned} \dot{x_{\text{dc}}} &= v^*_{\text{dc}} - v_{\text{dc}} \\ i^*_d &= K_{v_i} x_{\text{dc}} + K_{v_p}(v^*_{\text{dc}} - v_{\text{dc}}) \end{aligned} \tag{8}$$

where superscript "$*$" refers to the reference value. The dc voltage is called v_{dc} and x_{dc} is the additional state variable introduced by the PI controller. The output i^*_d of this controller is the reference for the d-axis current controller, and K_{v_p} and K_{v_i} are the proportional and integral gains, respectively.

The unfiltered q-axis current reference is generated by an outer droop-based controller that injects reactive power according to the voltage level at the point of connection. The control law can be written as

$$i^*_q = K_v(v^*_{\text{ac}} - v_g) \tag{9}$$

where K_v is the droop gain, v_g is the voltage magnitude at the converter connection point, and v^*_{ac} is its reference value. This signal is filtered by using a low-pass filter with a time constant T_f. Combining the filtered current with (9), the state equation for the q-axis reference current is derived

$$\dot{i^{*f}_q} = \frac{1}{T_f}(i^*_q - i^{*f}_q) = \frac{1}{T_f}(K_v(v^*_{\text{ac}} - v_g) - i^{*f}_q). \tag{10}$$

The dq current references are passed through the smooth saturator introduced in (7) in order to respect the current limits. This is mathematically expressed as

$$\begin{aligned} i^*_{d_{\text{sat}}} &= i^{\max}_d \tanh\left(i^*_d / i^{\max}_d\right) \\ i^{*f}_{q_{\text{sat}}} &= i^{\max}_q \tanh\left(i^{*f}_q / i^{\max}_q\right) \end{aligned} \tag{11}$$

where the subscript "sat" stands for the corresponding saturated variable. For the upper and lower saturation points, a dynamic limiting strategy is used. Specifically, the limiting scheme prioritizes the d-axis current (related to active power), while the rest of the available capacity is left free for injecting q-axis current (related to reactive power) [53]. This strategy ensures that all the converter capacity is used for maintaining the dc-voltage constant whenever needed and guarantees that loads remain fully supplied regardless of the voltage level. During disturbances on the dc-side (e.g., a load change), the full converter capacity may be required; otherwise, the dc voltage would decrease, and then, the dc load may be disconnected. The remaining current capacity of each converter can then be used for the grid support. The selection of this strategy is consistent with the assumption that the system retains equilibrium, even for large change of parameter values. It is also consistent with converter interconnection guidelines under the continuous operation region defined in [54]. Under fault conditions or large dynamic disturbances on the ac side, different strategies should be considered (e.g., prioritizing reactive power over active power) [55], [56].

This strategy can be mathematically expressed as follows:

$$i_d^{\max} = \pm I_{\lim}$$
$$i_q^{\max} = \pm\sqrt{I_{\lim}^2 - (i_{d_{\text{sat}}}^*)^2}. \tag{12}$$

By feeding the current references to the inner current controllers, the state equations of the PIs are defined. As shown in Fig. 2, the outputs of the current controller (v_{t_d} and v_{t_q}) are then added to the measured voltage of the connection point, together with appropriate decoupling terms [42]. The dynamic equations for current loops, dc capacitor, ac filter, and the process of deriving them are presented in the Appendix.

In order to take into account the converter losses, ac circuit and switching losses have been included in the model [57], [58]:

$$P_{\text{losses}} = (3/2)R_f i_{\text{ac}}^2 + G_{\text{sw}}(i_{\text{dc}})v_{\text{dc}}^2 \tag{13}$$
$$G_{\text{sw}}(i_{\text{dc}}) = G_0(i_{\text{dc}}/i_{\text{dc}}^{\text{nom}})^2 \tag{14}$$

where G_0 is a constant conductance and $i_{\text{dc}}^{\text{nom}}$ is the nominal dc current.

The SRF for each converter is obtained by using a PLL that aligns the d-axis with the grid voltage space vector. The mathematical description of the PLL is included in Section A of the Appendix.

C. Transformer With LTC

Transformers with LTCs are commonly used in electrical transmission and distribution systems. In electrical distribution systems, their rated power is proportional to the power of the feeder. Their objective is to regulate the voltage in the grids by mechanically adjusting the transformer ratio. In field applications, this adjustment is performed in discrete steps based on the available tap positions [7]. A continuous model has been used in this article, although the implementation in the laboratory is done in discrete time steps. The efficacy of the continuous-time approximation has already been validated in the literature [7].

A smooth saturator like the one presented in (6) has been used so that the tap ratio does not increase beyond its maximum value. The modeling equations are

$$v_l = a_{\text{sat}} v_h \tag{15}$$
$$\dot{a} = \frac{1}{T_{\text{ltc}}}(v^* - v_l) + \frac{1}{T_w}(a_{\text{sat}} - a) \tag{16}$$
$$a_{\text{sat}} = \frac{1}{2}[(a_{\max} + a_{\min}) + (a_{\max} - a_{\min})\tanh(s_g(a - a_n))] \tag{17}$$

where a is the continuous tap ratio, a_{sat} is its saturated value, v_l is the transformer low voltage, v_h is the transformer high voltage, v^* is the voltage control setpoint, T_{ltc} is the LTC time constant, $[a_{\min},\ a_{\max}]$ is the available range for the continuous tap ratio, a_n is the nominal tap ratio value, and s_g is the hyperbolic tangent function slope. The first term of (16) acts as an integral control on the voltage. Therefore, saturating the output of this equation would generate an effect similar to traditional "windup" on PI controllers. Thus, the unsaturated variable would increase indefinitely and the model would not converge. For this reason, the second term is added. This term circumvents the undesired effect and allows proper numerical integration. The combination of the saturation function together with the antiwindup term is first introduced in this article. In Fig. 4, the operation of the LTC is illustrated by using a block diagram that clearly resembles the scheme of an antiwindup mechanism [50]. The time constant T_w sets the time for a to reach the steady state when it saturates. Its value will not modify the system operating point, but it should be slow enough so that it does not interact with the rest of dynamic equations.

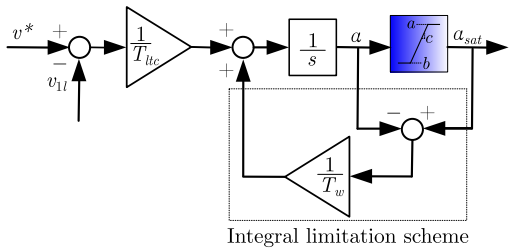

Fig. 4. Equivalent control scheme for the LTCs.

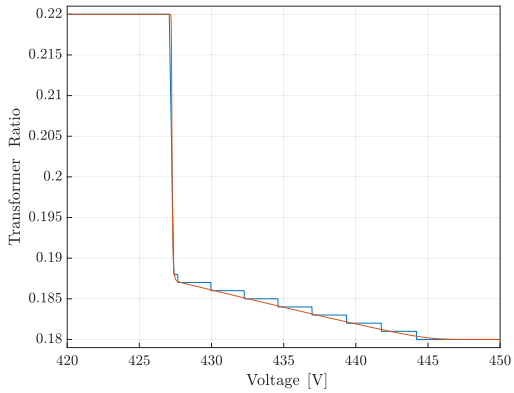

Fig. 5. Tap positions of (blue) discrete and (red) continuous LTC models, subject to a ramp increase in the regulated voltage.

In order to illustrate the operation of the transformer with the LTC, Fig. 5 shows the tap positions of the (blue) discrete and (red) continuous models when a ramp increase of the regulated voltage is imposed. It can be seen that the continuous model approximates well the realistic discrete model. Fig. 6 shows how parameters T_w and s_g affect the approximation. Careful tuning of these parameters should be considered so that the approximation error is minimized. More information regarding LTC modeling can be found in [7].

D. Electrical Lines

Electrical lines have been modeled by using a π-equivalent such as the one depicted in Fig. 7 [59]. In many bifurcation studies, line dynamics are considered to be faster than the rest of the system dynamics and are, therefore, simplified. However, they have been included in this article in order to keep the model fully differential and, therefore, avoiding algebraic constraints as

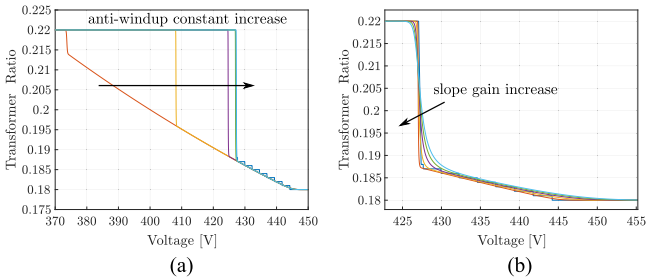

Fig. 6. Tap positions of discrete and continuous LTC models subject to a ramp increase of the regulated voltage. Comparison of continuous and discrete LTC models for variations of parameters (a) T_w and (b) s_g.

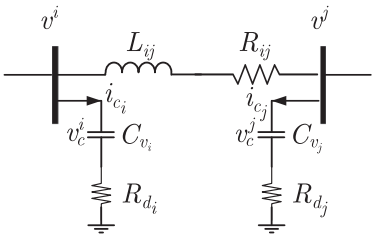

Fig. 7. Equivalent circuit for modeling electrical lines.

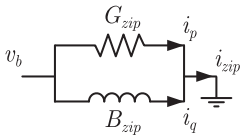

Fig. 8. Equivalent circuit of a ZIP load.

in (2). This simplifies the model definition in mathematical tools. Furthermore, the RC branches improve the problem resolution. First, small virtual capacitors accelerate the resolution with a negligible impact on the final result. Then, the resistors are calculated so that capacitors do not generate high-frequency resonances that would lead to oscillations in electrical waveforms. The line equations are presented in Section B of the Appendix.

E. Load Modeling

Loads have a significant impact on voltage stability [10]. In this work, the load was modeled by using a ZIP equivalent and an induction machine.

1) ZIP Load: ZIP loads can represent a variety of loads encountered in real systems. In this article, the ZIP load was modeled as in [22]. A parallel combination of nonlinear conductance G_{zip} and susceptance B_{zip} is used, as shown in Fig. 8. The equations are included in Section C in the Appendix.

2) Induction Motor: For the IM, both stator and rotor circuit dynamics are considered [60]. The equivalent circuit used in this study is depicted in Fig. 9 [60]. Since the IM model does not contain angle dynamics, the state variables can be directly added to the grid equations without transforming equations from one reference frame to another [61]. See Section D in the Appendix for more details.

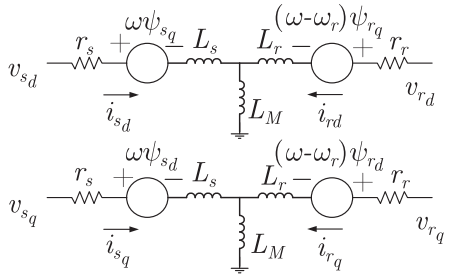

Fig. 9. Equivalent circuit of an IM.

TABLE I
HARDWARE AND CONTROL PARAMETERS OF VSCS

Parameter	Value	Parameter	Value
L_{f1},L_{f2}	3.23 mH	K_p^{pll}, K_i^{pll}	0.05, 0.95
R_{f1},R_{f2}	0.2255 Ω	C_{dc1},C_{dc2}	2 mF
K_{i_p}, K_{i_i}	5.79, 623.63	P_{dc1},P_{dc2}	7 kW
K_{v_p}, K_{v_i}	0.03, 0.92	V_{dc1},V_{dc2}	680 V
G_0	0.005	i_{dc}^{nom}	22.05 A

TABLE II
LOAD PARAMETERS

ZIP Load	Value	IM	Value
P_0	15 kW	J	0.554 kgm^2
Q_0	5 kvar	L_m	124.9 mH
a_1,a_2,a_3	0.2, 0.3, 0.5	L_s,L_r	2.9 mH, 2.9 mH
b_1,b_2,b_3	0.2, 0.3, 0.5	r_s,r_r	0.261 Ω, 0.684 Ω
T_i	0.001 s	K_0,K_1,K_2	21.67, 0, 0

IV. ANALYTICAL RESULTS

In this section, the electrical distribution system shown in Fig. 1 is analyzed. The system equations are obtained by using the procedure presented in Section III. Then, the bifurcation curves are calculated by using *Matcont*. Specifically, the process to obtain the bifurcation curves was the following.

1) The system was defined as a set of ordinary differential equations and then included in the *Matcont* file.
2) The system parameters were selected, as well as a generic initial point.
3) A time-domain simulation was performed using Simulink, until the system settles to an equilibrium.
4) Starting from the equilibrium point, a free parameter was selected in *Matcont*. Then, a parametric continuation analysis was performed until a BP was found.
5) If necessary, starting from the located BP, continuation in two dimensions was performed by selecting two free parameters.

The validity of the hyperbolic saturation model is first established, and then, the model is used for the system analysis. The numerical values of the converter parameters, the load, and the rest of the network elements are shown in Tables I–III, respectively. These were the parameter values that were used to obtain the initial equilibrium point of the system. If not stated otherwise, the saturation limits of the LTC tap ratio are set to

TABLE III
GRID AND TRANSFORMER PARAMETERS

Parameter	Value	Parameter	Value
S_{base}	50 kVA	V_{base}	2 kV
V_{g_d}	2 kV	V_{g_q}	0 V
L_g	50 mH	R_g	2.62 Ω
	0.196 p.u.		0.032 p.u.
L_{ltc}	0.4 mH	R_{ltc}	0 Ω
	0.039 p.u.		0 pu
L_{23}	1 mH	R_{23}	0.333 Ω
	0.098 p.u.		0.104 p.u.

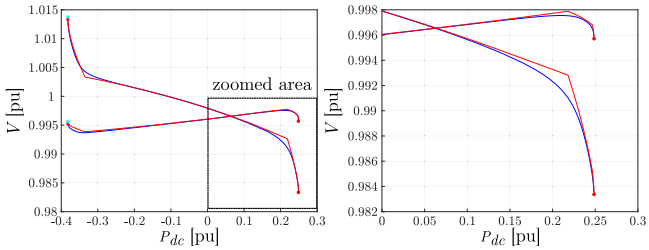

Fig. 10. Bifurcation diagram of the voltages of Nodes 2 and 3 when the dc power is modified. Full and zoomed versions.

10%, and the converter current limits are set to the nominal value of the converter current. PI controllers have been designed so that responses comply with standard transient specifications under nominal conditions. Specifically. the damping is set to 0.7, while the settling times are set to 7 ms and 70 ms for current and dc voltage PIs, respectively. PLL bandwidths are set to 60 Hz.

A. Saturation Modeling Validation

Fig. 10 (left) compares the different curves of the system when saturators are modeled using (blue) hyperbolic tangent functions and (red) regular nonsmooth saturators. It can be seen that the equilibrium values are tracked only with small errors around the saturation "knee." When the dc load increases (positive values), both models predict the BP at almost the same value. On the power injection side (negative values), the BP is also identified by using the hyperbolic tangent approximation. However, the nonsmooth version is numerically unstable, and the simulation collapses at the point marked using the cyan asterisk. Fig. 10 (right) shows the detailed view near the saturation point to emphasize the minimal error in the equilibrium values.

Fig. 11 shows the case in which the active power of the load is increased. In this case, only the LTC and q-axis current limits affect the system operation as the d-axis current demanded by the converters remains unchanged. The location of the collapse point, marked by the red asterisk, remains almost unaffected. For the equilibrium values, there are three points, in which different limitations are met. At $P_o \approx 1.6$ p.u., the LTC limits are met, and it can no longer regulate the grid voltage. At this point, the network voltages start to decrease. At points $P_o \approx 2.25$ p.u. and $P_o \approx 2.4$ p.u., the q-axis current limits of Converters 1 and 2 are, respectively, met and, without reactive support, the voltage

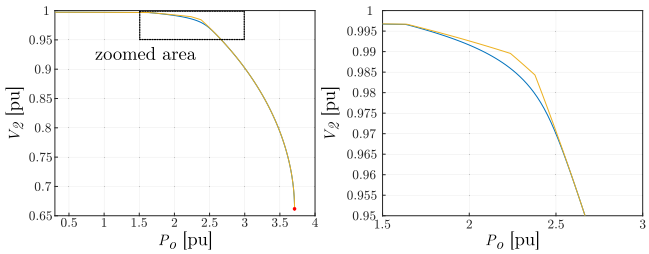

Fig. 11. Bifurcation diagrams of Node 2 voltage when the ac load is changed. (Yellow) Piecewise linear saturation and (blue) approximate saturation. Full and zoomed versions.

reduction becomes sharper. In the first case, the approximation gives accurate results. At the following points, shown in the zoomed version of Fig. 11, the error slightly increases but never exceeds 0.5%. It is worth pointing out that this small error can be further decreased by adjusting the slope s_g in (17) if the minimum error around the "knee" is favored over adaptability and tuning simplicity. It is also important to mention that the error produced by the adopted approximation is, in the general case, lower than the expected error in real measurements due to inherent noise, component uncertainty, etc.

B. Bifurcation Analysis

To validate the main contributions of this article, the following scenarios are studied.

1) *Effect of the VSC capacity limit with the dc load variation:* In this case, the effect of the power absorbed/injected by the VSCs is studied. This scenario demonstrates the nonlinear effects of VSCs as well as the impact of converter capacity limits on the system stability.
2) *Effect of the LTC limits and weak grid conditions:* Weak interconnections are explored by varying the short-circuit ratio (SCR) of the grid. Different R/X ratios are used to see the effect of inductive and resistive grids (the latter case is common in low-voltage networks).
   Different LTC limits and their effects are also studied. The ability of converters to regulate the voltage will also be analyzed.
3) *Nonlinear effect of converter control parameters:* Variation of controller parameters may lead to sudden loss of stability through HBs, without previous changes in the equilibrium variable values. Hence, nonlinear analysis is necessary. Here, parametric continuation is applied to the voltage controller droop gain and other control parameters in order to provide insight in reactive power support requested from converters. The results can be used to adequately design the droop coefficients as well as the PI gains.

1) Case 1: Effect of the VSC Capacity Limit With DC Load Variation: Fig. 12 shows the voltage of Node 3 when the dc power is varied from positive (load mode) to negative (source mode) values. To obtain this figure, continuation of parameter P_{dc} was performed in both increase and decrease directions. The process terminated when the first bifurcation was encountered

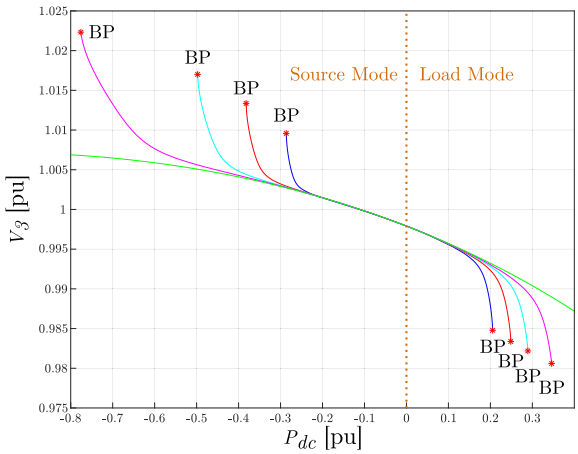

Fig. 12. Voltage of Node 3 when the dc power is changed. Current saturation limits were set to (blue) 80%, (red) 100%, (cyan) 120%, and (pink) 150% of the rated converter capacity. The operation of the system when no limits are imposed is shown in green. BPs are marked with a red asterisk.

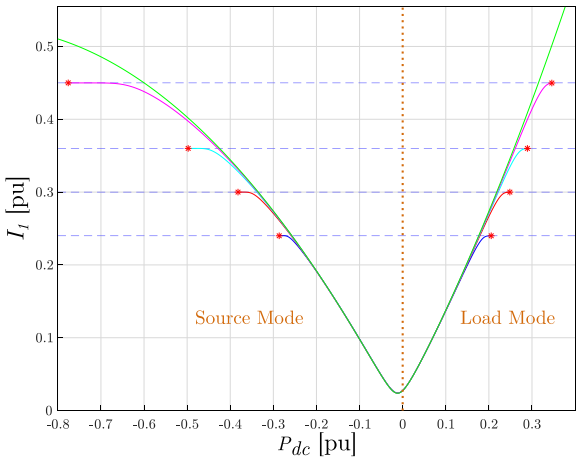

Fig. 13. rms current of Converter 1 when the dc power is changed. Current saturation limits were set to (blue) 80%, (red) 100%, (cyan) 120%, and (pink) 150% of the rated converter capacity. The operation of the system when no limits are imposed is shown in green. BPs are marked with a red asterisk.

in each direction. The voltage rms value v_3 was calculated from the voltage dq components with the formula: $v_3 = (v_d^2 + v_q^2)^{1/2}$. Because Node 3 is "electrically remote" from the ideal grid, the voltage levels mostly depend on the converter operation. Therefore, over- and undervoltages will take place depending on the power flow direction. BPs appear in both directions, but the limits are not symmetrical. In addition, it can be seen that the system may become unstable even if the node voltage is kept within adequate limits. To investigate the effect of the converter capacity limits, the process is repeated for several values of maximum allowed converter current. For each iteration, the current saturation limits were set to (blue) 80%, (red) 100%, (cyan) 120%, and (pink) 150% of the rated converter capacity, respectively. The case without current saturation is shown in green.

Fig. 13 shows the rms current of Converter 1 when the dc power is changed in either directions. The rms current

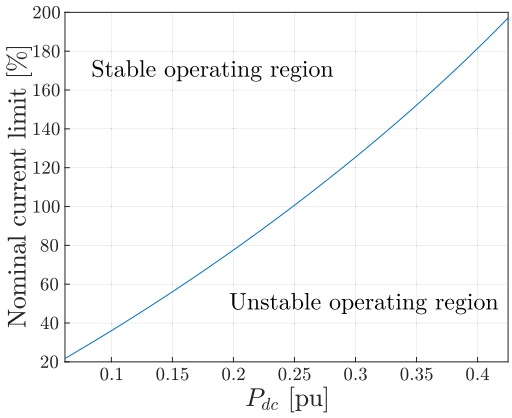

Fig. 14. Bifurcation diagram for simultaneous variation of $P_{\rm dc}$ together with converter capacity limit.

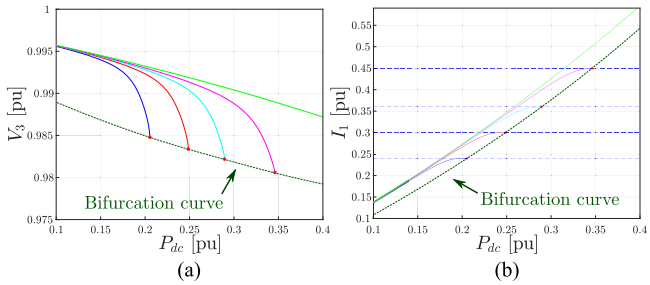

Fig. 15. Zoomed-in parts of (a) Fig. 12 and (b) Fig. 13. The bifurcation curves that monitor how the BP "moves" are additionally plotted with thick dashed lines.

of Converter 1 is calculated by using the following formula: $i_1 = (i_d^2 + i_q^2)^{1/2}$. In both load and source modes, the stability limits coincide with the rms current limits. The fact that the instability occurs when the total current reaches the limit and not when either d-axis or q-axis current is saturated justifies the inclusion of the dynamic limit modeling. This analysis also gives insight into the main factor behind the instability, namely, the current limit. This type of instability is a general case of the limit-induced instability recently reported in [35].

To examine the effects of the current limit on the bifurcation in more detail, additional parameter continuation was performed with *Matcont*. First, the initial bifurcation curve for nominal current limit was recalculated (red curve of Fig. 12, i.e., current limit 100%). Then, the current limit was selected as an additional free parameter with the BP being preserved. Fig. 14 shows how the BP changes when the dc load and the current limit are varied simultaneously, thus defining the parameter stability region. Fig. 15(a) projects the same multidimensional curve on the V_3–$P_{\rm dc}$ plane, while Fig. 15(b) projects it in the I_1–$P_{\rm dc}$ plane. Both figures provide insight into the relation between the BP and the current limit. Specifically, for the case where no limit is set (green curves of Fig. 15), it can be seen that the green curves and the bifurcation boundary diverge and they will not coincide for reasonable loading values within the system rating.

2) Case 2: LTC Limits and Weak Grid Conditions: Fig. 16 shows the voltage of Node 2 when (red) L_g and (black) R_g

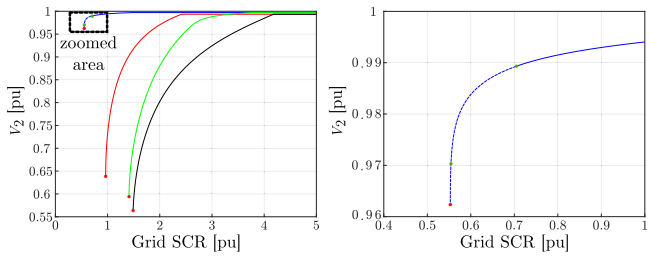

Fig. 16. Voltage of Node 2 when the SCR changes (inductive grid) with the droop controller (blue) enabled and (red) disabled. Same case for resistive grid, with droop (green) enabled and (black) disabled. (Red asterisk) SNB point and (green asterisk) HB points. Full and zoomed versions.

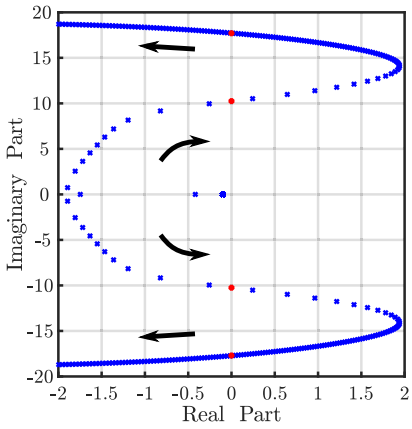

Fig. 17. Eigenvalues for variation of the grid inductance L_g, while the droop controller is active. The eigenvalues for which the HBs appear are denoted using a red asterisks.

are modified. No droop controller is used in this test. The SNB points are located at SCR $= 0.963$ for the inductive case and at SCR $= 1.489$ for the resistive case. In both cases, the system shows a similar trend. However, in the case of resistive weak grids, the bifurcation occurs for higher SCR values. Fig. 16 also shows the voltage of Node 2 when (blue) L_g and (green) R_g are modified. However, in this case, the reactive power support is activated. For inductive grids, the voltage profile is flat until stability is lost through an unstable HB at SCR $= 0.705$. This HB appears because of the interaction between the weak grid and VSCs controllers. It can be seen that, despite the undesirable interaction, the system stability margin has improved. A second HB is identified for a higher value of L_g, with no effect on the system stability. However, for a resistive interconnection, reactive power support does not have a significant impact and the system collapses at SCR $= 1.441$. Fig. 17 shows how the critical eigenvalues change in the case of the grid inductance variation and confirms the instability of the limit cycle that is generated at the identified HB. The double crossing of the imaginary axis by the eigenvalues is consistent with the two identified HB points.

To investigate the effect of the LTC limits, continuation was performed for different LTC regulating ranges. Fig. 18 shows the response of the system to the increase of the ac ZIP load value P_o with the tap ratio limit ranging from 0% to 15%. It can be seen that with bigger tap limit range, the drop of the voltage starts at a larger load value. However, the collapse point remains almost

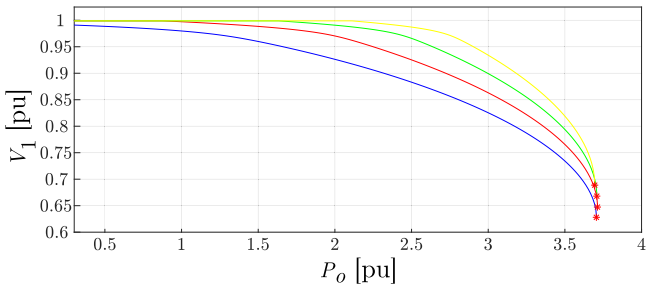

Fig. 18. Voltage of Node 1 when the active power load is increased. Tap limit is changed to (blue) 0%, (red) 5%, (green) 10%, and (yellow) 15%.

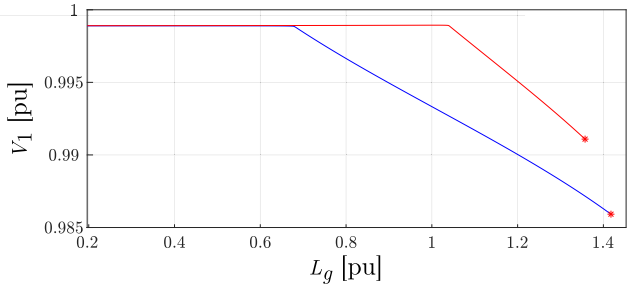

Fig. 19. Voltage of Node 1 when the grid inductance is increased. Tap limit is changed from (blue) 10% to (red) 30%.

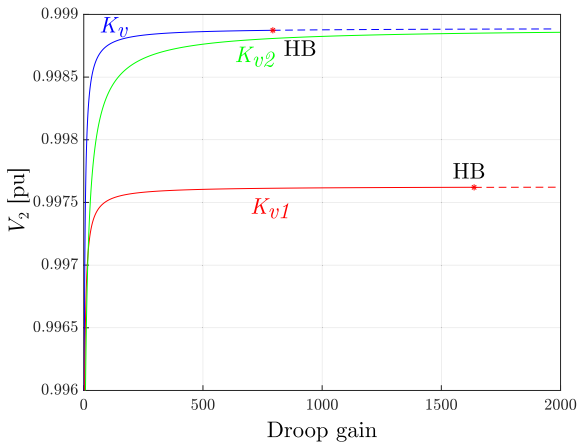

Fig. 20. Bifurcation diagram of the voltage of Node 2 when the q-axis current droop gain is increased for (red) Converter 1, (green) Converter 2, and (blue) simultaneous increase. Stable equilibrium is shown using a straight line, while unstable equilibrium is shown using a dashed line.

unaffected. Fig. 19 shows a weak inductive grid scenario. The response is similar to the previous case, and the collapse occurs at a slightly different inductance value, despite the significant extension of the LTC range capability (30%).

3) Case 3: Nonlinear Effect of Converter Control Parameters: Fig. 20 shows the effect of the variation of the droop coefficients on the voltage of Node 2. The cases of simultaneous variation of the droops (in blue) and their separate variation (in red and green) were studied. The former is often denoted as *symmetrical variation*, while the latter is denoted as *asymmetrical variation* [19]. It can be seen that the way these gains are

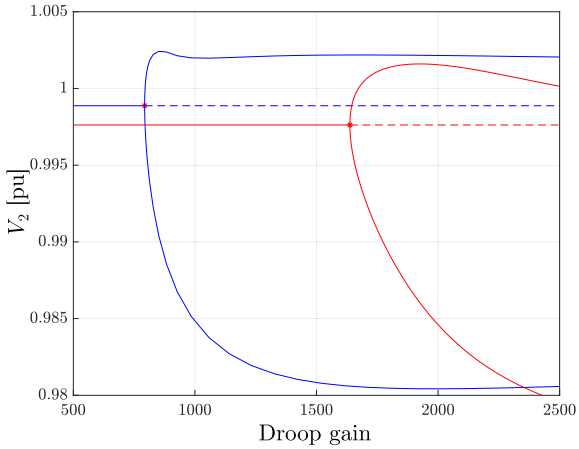

Fig. 21. Bifurcation diagram showing the amplitude of the limit cycles that emerge from the variation of the q-axis current droop gain of (red) Converter 1 and (blue) simultaneous variation.

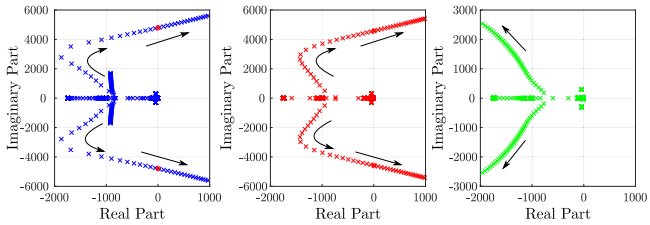

Fig. 22. Eigenvalues for variation of the droop gain of the outer voltage controller. Eigenvalues for (blue) simultaneous variation of droops, (red) Converter 1, and (green) Converter 2. "*" means "HB."

modified can have a significant impact on the system stability. The HBs in Fig. 20 appear for very large values of the droop gains, which are typically considered impractical.

Figs. 21 and 22 provide additional information regarding the encountered bifurcations. Fig. 21 shows the magnitudes of the limit cycles that are generated from the corresponding Hopf points. Fig. 22 shows the root locus diagram of the critical eigenvalues for each case. With them, the equilibrium stability can be determined. It can be seen that all the detected HBs lead to instability because the imaginary axis is crossed. In the final case, all the eigenvalues remain in the left-hand side confirming that stability is preserved. It can be seen that the frequency of the eigenvalues that move to the imaginary axis is very large, meaning that the oscillation will appear at high frequency. This is in line with the large value of the droop gain required to obtain the HB. If any of the resulting limit cycles is attractive, sustained oscillations appear in the system. For example, Fig. 23 shows Node 2 voltage after the dq components of Converter 1 current were perturbed at the HB encountered by the variation of droop gain k_{v1} (red curve of Fig. 20). It can be seen that sustained oscillations of small amplitude emerge and remain in the system, indefinitely. One should note that, despite the small amplitude of the oscillation, equilibrium stability is lost, and this is considered unacceptable for power system operation [7].

Fig. 24 shows how the HB produced from changing k_{v1} (red curve of Fig. 20) changes as a function of the line inductance L_{23}.

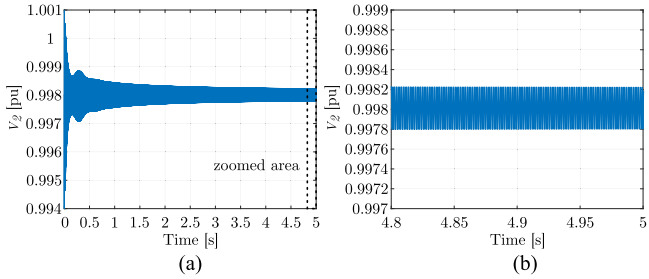

Fig. 23. Example of sustained oscillations in the system. Results from perturbation of Converter 1 dq-current components at the HB of the k_{v1}. (a) rms value of the voltage of Node 2. (b) Zoomed-in version.

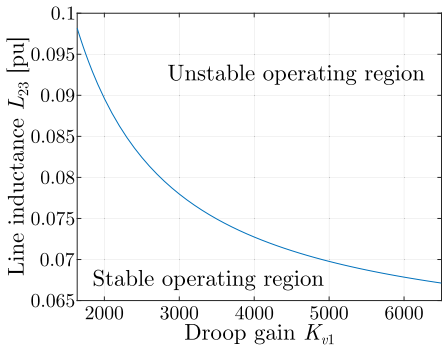

Fig. 24. HB boundaries when line inductance values L_{23} are changed together with Converter 1 droop gain K_{v1}.

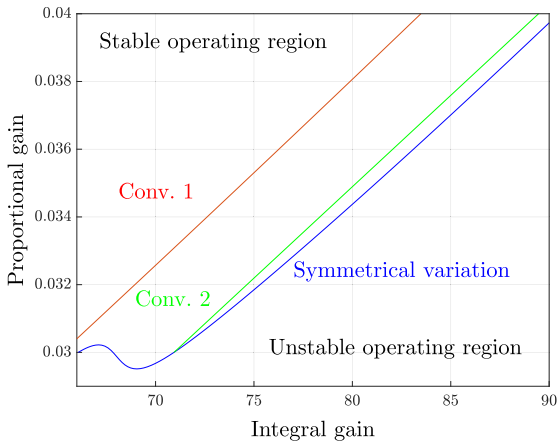

Fig. 25. HB boundaries when different sets of PI gains are selected for the dc voltage controller. Boundaries are shown for (red) Converter 1, (green) Converter 2, and (blue) simultaneous variation.

It can be seen that for lower induction values, the HB "moves" to higher gain values. This explains why there is no HB when k_{v2} is changed, namely, that the equivalent impedance to which the converter is connected to is lower and, thus, the electrical "distance" from the ideal grid shorter. This limits the undesirable interactions between the controllers and extends the parameter stability region.

Bifurcation analysis can also be used to calculate two parameter stability boundaries [19], [22]. Fig. 25 shows the Hopf

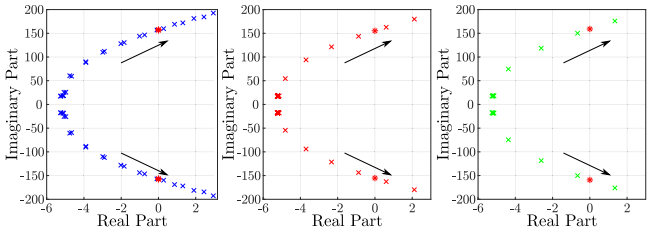

Fig. 26. Eigenvalues for variation of the integral gain k_{vi} of the dc voltage PI controller. Eigenvalues for simultaneous variation in (blue) both converters, (red) Converter 1, and (green) Converter 2. "*" means "HB."

Fig. 27. Photographs of the laboratory. (a) AC busbars. (b) 15-kVA converters. (c) Real-time computers. (d) 75-kVA converter. (e) Line impedances.

boundary that separates the stable and unstable operating regions when both proportional and integral gains K_{v_p} and K_{v_i} [in (8)] of the dc voltage controller are changed. Both symmetrical and asymmetrical variations are studied. It can be observed that the stable operation area is smaller for the converter that is electrically "more distant" from the ideal grid. In addition, the symmetrical variation introduces stronger nonlinear effects in the lower gain region. Fig. 26 provides the critical eigenvalues for the different cases. For the dc controller, the simultaneous variation of the integral gains (in blue) led to similar results as the independent variation of the same parameters in each converter (red and green). Two branches of the root locus move almost in parallel and cross the imaginary axis in close succession. Together with the results from Fig. 22, it can be concluded that the operation during symmetrical variation can be represented as the superposition of the asymmetrical cases. One should note that the detected Hopf bifurcation appears at high frequency because of very large values of the droop gains. Operation close to this region should be avoided in field applications.

V. Experimental Validation

A. Prototype Description

The theoretical results were validated in the Smart Energy Integration Lab (SEIL) [62], [63]. Fig. 27 shows a photograph of the experimental platform used for the experiments, while

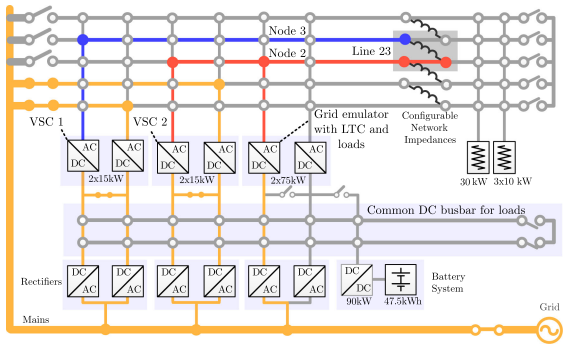

Fig. 28. Single-line electrical diagram of the laboratory facilities, including the test network configuration setup. Different colors represent different points of common voltage in the grid.

Fig. 28 shows the electrical single-line diagram of the laboratory configuration used for the reproduction of the test network shown in Fig. 1. Yellow, red, and blue paths define points in the network with common voltage. In particular, red represents the laboratory equivalent of Node 2 of Fig. 1, blue represents Node 3 of Fig. 1, and yellow represents the auxiliary grid voltage. Embedded PCs were used for the implementation of the control systems for all converters [63]. Two sets of 15-kVA back-to-back converters were used as the VSC-interfaced elements of Fig. 1. One terminal was connected to the test network and included the control loops, as shown in Fig. 2, while the other was connected to the auxiliary grid and emulated the dc load. Converters were connected to the grid by using *LCL* filters. *LCL* filter capacitors were small (8.8 μF), and therefore, their effect was negligible. The current saturation and the LTC saturation were implemented by using ideal saturation blocks (not smooth saturators), in the same way as in real field applications. The fact that the errors recorded during the experimental validation never exceeded 10% validates the hypotheses used in the theoretical analysis. The sampling and switching frequencies were set to 10 kHz. Pulsewidth modulation with the min–max modulation strategy and the single update was used [42]. The values of the components are provided in Table I.

The grid, the grid impedance, the mixed load, and the LTC transformer were emulated by using a 75-kVA VSC grid emulator. Therefore, this emulation defines a power-hardware-in-the-loop (PHIL) test of the grid defined in Fig. 1. To summarize, all the components left of Node 2 in Fig. 1 were included in the PHIL configuration. The rest of the system converters, as well as the line impedance, were represented by real laboratory hardware. The equivalent laboratory components that represent the test system components (e.g., VSC 1, Line 23, etc.) are also depicted in Fig. 28. The converter that emulated the grid included an LC output filter ($L_f = 500$ μH and $C_f = 100$ μF). The filter capacitor was controlled by using a fast full state-feedback controller so that the LC filter does not interact with the rest of the system. For the tap modeling, a realistic discrete-time model was used [7]. The voltage of Node 2 was calculated from the mathematical model (included in the grid emulator) and then used as an input for the voltage controller [64]. The distribution

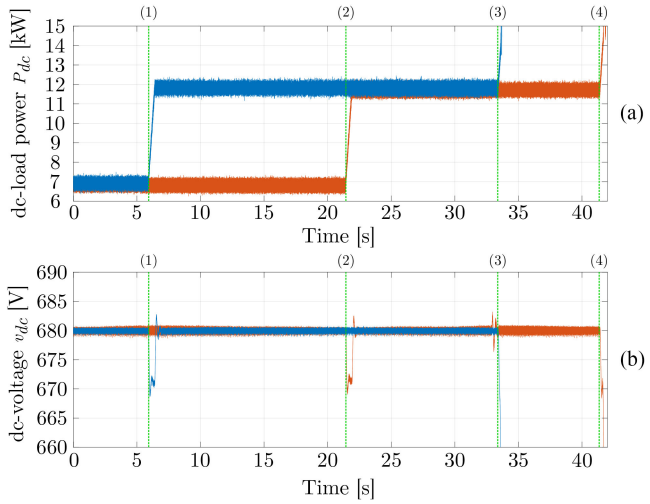

Fig. 29. Experimental verification for Case 1. (a) DC load power and (b) dc voltage of each converter.

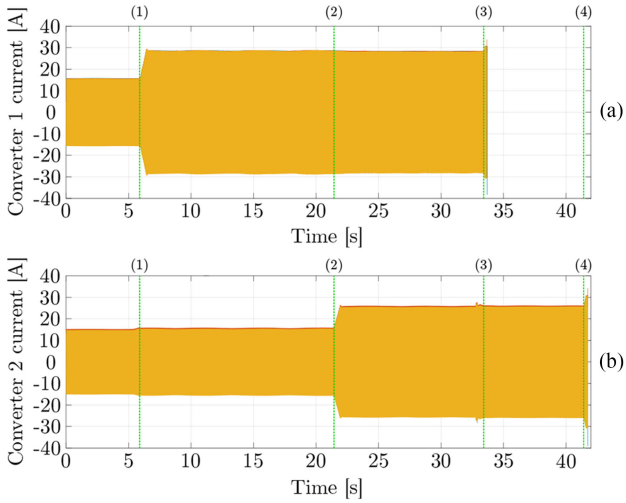

Fig. 30. Experimental verification for Case 1. (a) Current of Converter 1. (b) Current of Converter 2.

line in Fig. 1 was implemented by using a set of configurable impedances with values of $L_{\text{line}} = 1$ mH and $R_{\text{line}} = 0.3\ \Omega$.

B. Experimental Results

To validate the performed analysis, experiments for each test case described in Section IV-B were performed. The converter voltage support capability was active in all experiments, unless it was explicitly stated otherwise. Similarly, the tap limit was set to 10% of its nominal value, and the converter current limit was set to its rated current value.

1) Case 1: In Fig. 29, the experimental results for Case 1 are shown. Fig. 29(a) shows the dc load power P_{dc} that is fed by the two converters, while Fig. 29(b) shows the voltage at the two dc links. At point 1, the active power demanded by Converter 1 was increased from the equilibrium conditions to a level close to the limit that was theoretically predicted (12 kW), but without exceeding it. The same action was performed for Converter 2 at point 2. In both cases, it can be seen that the dc voltage was restored to the nominal value after the initial transient. At point 3, the active power demand was increased beyond the predicted stability limit for Converter 1. At this point, the dc voltage sharply decreased and the controller was not able to restore it, leading to the converter disconnecting. At point 4, the action was repeated for Converter 2 with similar results. Fig. 30(a) shows Converter 1 current and Fig. 30(b) shows Converter 2 current. The increase in the current amplitude at points 1 and 2 is caused by the increase of the respective dc loads. At points 3 and 4, current is saturated at its maximum value of 30.61 A. Then, the respective converters are quickly disconnected because the dc-voltage protection tripped.

2) Case 2: Figs. 31– 34 show the recreated conditions of the collapse for Case 2 (gradual increase of L_g). To approximate the preservation of equilibrium during the parameter continuation, slow ramp increase of the parameter followed by quantization in steps of 1 mH was performed. Therefore, all the variables settled before the next step ensuring that transient effects did not affect the result. This also ensured that stability was not lost at an earlier point for any reason unrelated to the system loading (e.g., loss of synchronism by the converters). Fig. 31(a) demonstrates the rms voltage of Node 2 during this increase. It can be seen that despite the gradual increase in the grid inductance, the

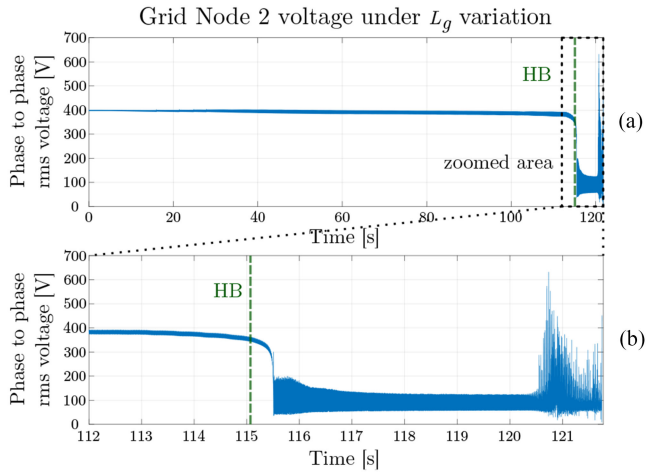

Fig. 31. Experimental verification for Case 2. (a) Node 2 rms voltage for variation of L_g and (b) zoomed area. HB is marked with a vertical, dashed, green line.

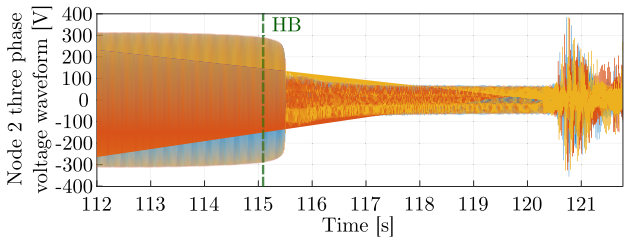

Fig. 32. Experimental verification for Case 2. Node 2 measured voltage waveforms. HB is marked with a vertical, dashed, green line.

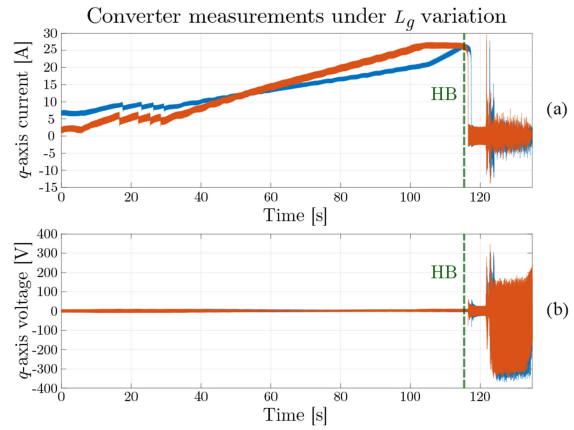

Fig. 33. Experimental verification for Case 2. (Blue) Converter 1 measurements and (red) Converter 2 measurements. (a) q-axis current measurements and (b) q-axis voltage measurements. HB is marked with a vertical, dashed, green line.

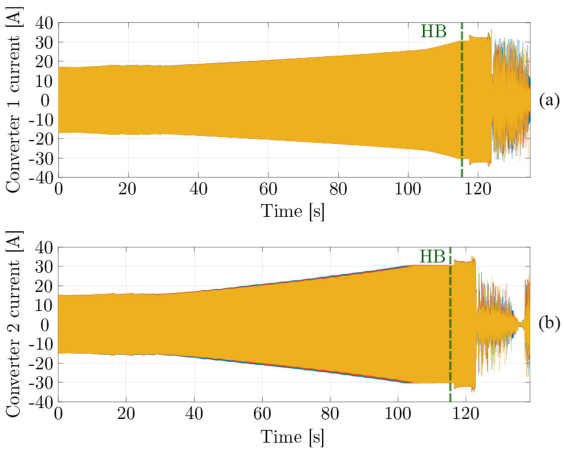

Fig. 34. Experimental verification for Case 2. Three-phase current waveforms of (a) Converter 1 and (b) Converter 2. HB is marked with a vertical, dashed, green line.

voltage remained close to its nominal value, as predicted in Fig. 16. At a point near the HB, there was a sharp nonlinear decrease in the voltage, after which unstable oscillations appeared and the converters were disconnected for protection. Fig. 31(b) shows a zoomed-in version near the collapse point. Fig. 32 shows the respective three-phase voltage measurements near the collapse point. Fig. 33(a) shows the q-axis current of the two converters during the experiment. It can be seen that at the initial stages (15–30 s), the current is quickly adjusted due to the LTC voltage regulation. Once the LTC capability is depleted, the current steadily rises due to the voltage drop at the converter terminals. After the instability, it quickly drops to zero due to the current saturation scheme. Fig. 33(b) shows the q-axis voltage component, as measured in the reference frame of each converter. It can be seen that the converter PLLs successfully keep these components close to zero for the majority of the experiment, thus maintaining synchronization. Near the collapse point, the grid voltage decreases rapidly and the PLLs are incapable of preserving synchronization. This also justifies the step-like decrease in the grid inductance L_g, as it

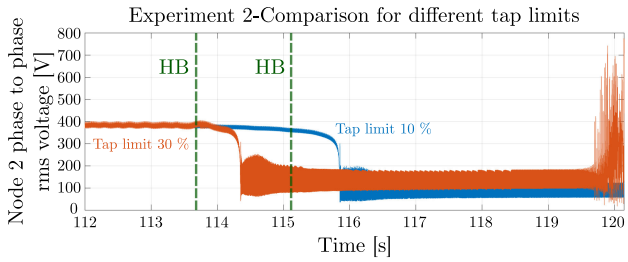

Fig. 35. Experimental verification for Case 2. Comparison for different tap limit ratios. (Blue) Tap limit 10% and (red) tap limit 30%. HBs are marked with a vertical, dashed, green line.

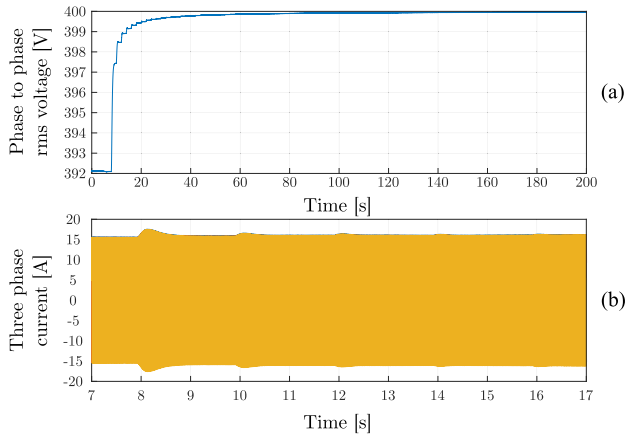

Fig. 36. Experimental verification for Case 3. (a) Node 3 rms voltage for variation of K_{v1}. (b) Measured current waveforms of Converter 1.

becomes clear that the stability is lost through the HB. When this bifurcation is reached, the whole system collapses, and then, the PLL loses synchronization. Fig. 34 shows the three-phase current waveforms of the converters for this experiment.

For completeness, the same experiment was repeated for the tap limit ratio set to 30% of its nominal value. That way, a direct comparison between the cases can be conducted. Fig. 35 shows Node 2 voltage for tap limit 10% (blue) and 30% (red) and identical increase of grid inductance L_g. The figure has been zoomed in for clarity to show the region near the collapse point. It can be seen that despite the larger LTC capability, the collapse occurs at slightly reduced inductance value, as predicted in Fig. 19.

3) Case 3: For the validation of Case 3, an experiment reproducing the equilibrium curve from Fig. 20 for small values of K_{v1} was performed. Starting from the initial equilibrium condition ($K_{v1} = 0$), the droop gain was increased every 2 s until $K_{v1} = 100$. Fig. 36(a) shows the increase in the rms voltage of Node 3 originating from the increased reactive power support offered by Converter 1. Fig. 36(b) shows the measured three-phase current injected by the converter during the initial transients. After the voltage measurements were filtered and averaged to clear out any noise, they were compared with the theoretical curve, as shown in Fig. 37(a). It can be seen that the measured results closely match the respective theoretical values with the relative error [shown in Fig. 37(b)] never exceeding

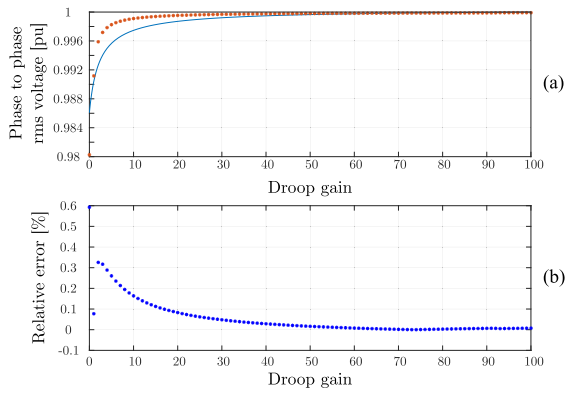

Fig. 37. Validation of results for Case 3. (a) Comparison between (blue) theoretical and (red) experimental results. (b) Relative error between the two.

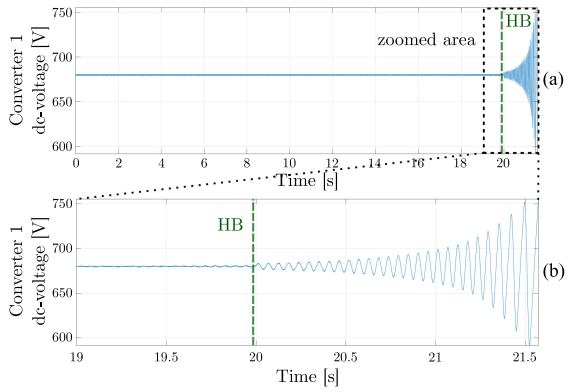

Fig. 38. Experimental results for Case 3. (a) DC voltage of Converter 1 when the integral gain of the dc-voltage controller is incrementally modified. (b) Zoom in close to the instability point. HB is marked with a vertical, dashed, green line.

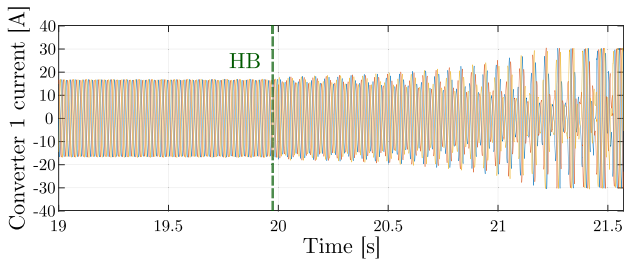

Fig. 39. Experimental results for Case 3. Three-phase current waveform of Converter 1, while the integral gain of the dc-voltage controller is incrementally modified. Zoomed-in figure near the point at which stability is lost. HB is marked with a vertical, dashed, green line.

1% and tending to zero as the droop gain increases. In a similar manner, Converter 1 integral gain of the dc-voltage controller k_{vi} was slowly increased until the HB was encountered. Fig. 38(a) and its zoomed-in part in Fig. 38(b) show the dc-voltage of Converter 1 during the experiment. Despite the gain increase, the dc-voltage remains constant and equal to the reference value (680 V). After the predicted HB, oscillations of growing amplitude appear and the converter is soon disconnected for protection. Fig. 39 shows the three-phase current measurement of the same converter during the experiment. It is zoomed in for clarity to show the region close to the disconnection point. The oscillations appear in the ac part due to the modulation process.

VI. Conclusion

In this article, bifurcation theory was used to perform nonlinear analysis of parameter stability in active electrical distributions systems, including the effects of the LTCs and the converter capacity limits. This represents a novel approach to stability analysis of grid-connected, converter-dominated, active distribution systems. First, the necessary models of these network elements for the nonlinear study were developed. Then, numerical bifurcation theory was used to study the power transfer limits and parameter stability boundaries in the grid. A test system comprising power converters, a ZIP load, an IM, and electrical lines was modeled and studied in detail. The effect of controller parameters on network stability was explained and presented. In addition, converter capacity limits and the effects attributed to weak grid conditions were analyzed. Finally, the theoretical developments were validated by using experimental results.

The obtained results confirmed the proposed modeling approach that successfully approximates the operation of LTCs and saturation blocks, allowing their inclusion in nonlinear bifurcation studies. In the case of the dc load increase, it was found that the upper limit of the rms converter current acts as the stability limit for the whole system. This effect is reminiscent of limit-induced bifurcations. Reactive power support provided by electronic interfaces proved helpful in the case of inductive weak grids since it flattened the voltage profile. However, in predominantly resistive interconnections, there was no notable improvement. LTC limits were shown to affect the equilibrium values of the system voltage, but their effect on the location of the collapse point was minimal. It was shown that variation of both droop and PI gains may lead to HBs. For most test cases, different dynamic responses were observed after applying the changes to the controller gains simultaneously and separately. Finally, the experimental results from the tests performed in the SEIL were used to validate the proposed modeling approach and the obtained analytical results.

Appendix
Supplementary Modeling Equations

In this appendix, the models of the VSC, the loads, and the electrical lines are given.

A. VSC Modeling

The state equations for the PIs of the inner current control loops are

$$\begin{aligned} \dot{x_d} &= i^*_{d_{\text{sat}}} - i_d \\ \dot{x_q} &= i^{*f}_{q_{\text{sat}}} - i_q. \end{aligned} \tag{18}$$

The equations for the terminal voltages of the converters are

$$\begin{aligned} v_{k_d} &= v_{t_d} - L_f \omega i_q + v_{g_d} \\ v_{k_q} &= v_{t_q} + L_f \omega i_d + v_{g_q} \end{aligned} \tag{19}$$

where L_f is the induction of the converter filter. By applying Ohm's law to the impedance of the filter and canceling out the feedforward term, the dynamic equations of the currents of the converter are derived

$$\dot{i_d} = -\frac{R_f}{L_f} i_d + \frac{K_{i_p}}{L_f}(i^*_{d_{\text{sat}}} - i_d) + \frac{K_{i_i}}{L_f} x_d$$
$$\dot{i_q} = -\frac{R_f}{L_f} i_q + \frac{K_{i_p}}{L_f}(i^{*f}_{q_{\text{sat}}} - i_q) + \frac{K_{i_i}}{L_f} x_q \tag{20}$$

where K_{i_p} and K_{i_i} represent the proportional and integral gains of the current controller, respectively. From the energy conservation principle, the dc-side dynamics are derived

$$\dot{v_{\text{dc}}} = \frac{1}{v_{\text{dc}} C_{\text{dc}}}(P_{\text{ac}} - P_{\text{dc}} - P_{\text{losses}})$$
$$= \frac{3}{2 v_{\text{dc}} C_{\text{dc}}}(u_{k_d} i_d + u_{k_q} i_q) - \frac{P_{\text{dc}}}{v_{\text{dc}} C_{\text{dc}}} - \frac{P_{\text{losses}}}{v_{\text{dc}} C_{\text{dc}}} \tag{21}$$

where P_{ac} and P_{dc} are the power that enter or exit the dc link from the ac and dc sides, respectively.

An internal state is introduced for the PI controller of the PLL. Together with integral and proportional gains $K_i^{\text{pll}}, K_p^{\text{pll}}$, the dynamics of the PLL are defined as

$$\dot{x_{\text{pll}}} = v_{g_q} \tag{22}$$
$$\dot{\delta} = \omega_{\text{pll}} = K_i^{\text{pll}} x_{\text{pll}} + K_p^{\text{pll}} v_{g_q}. \tag{23}$$

B. Model of Electrical Lines

The equations for the current of a line connecting node i to node j are

$$\dot{i_d} = \frac{v_d^i}{L} - \frac{v_d^j}{L} - \frac{R}{L} i_d + \omega i_q$$
$$\dot{i_q} = \frac{v_q^i}{L} - \frac{v_q^j}{L} - \frac{R}{L} i_q - \omega i_d \tag{24}$$

where R and L are the lumped resistive and inductive parameters of the line, respectively. To define node voltages, virtual shunt capacitors are used. Their dynamics are described as

$$\dot{v_{c_d}} = \omega v_{c_q} + \frac{\sum_{j \in \text{node}} i_{d_j}}{C_v}$$
$$\dot{v_{c_q}} = -\omega v_{c_d} + \frac{\sum_{j \in \text{node}} i_{q_j}}{C_v} \tag{25}$$

where C_v is a virtual capacitor that has been added in order to speed up the resolution of dynamic equations.

The node voltages are

$$v = v_c + R_d \cdot \sum_{j \in \text{node}} i_j \tag{26}$$

where R_d is a damping resistor that has been added in order to avoid high-frequency oscillations generated by the virtual capacitors. The signs of the currents that are added in (25) and (26) depend on the system topology.

C. ZIP Load Model

The equations of the nonlinear conductance G_{zip} and susceptance B_{zip} of Fig. 8 are given as

$$G_{\text{zip}} = P_0 \left(\frac{a_1}{V_0^2} + \frac{a_2}{V_0 V_b} + \frac{a_3}{V_b^2} \right)$$
$$B_{\text{zip}} = -Q_0 \left(\frac{b_1}{V_0^2} + \frac{b_2}{V_0 V_b} + \frac{b_3}{V_b^2} \right) \tag{27}$$

where P_0 and Q_0 are the active and reactive power consumption for nominal voltage V_0, respectively. V_b is the load voltage module, and indices a_1 and b_1 to a_3 and b_3 are the percentages of constant impedance, constant current, and constant power, respectively. The dynamics of the load current are calculated as follows:

$$\dot{i_{pd}} = \frac{G_{\text{zip}} v_d - i_{pd}}{T_i}, \quad \dot{i_{pq}} = \frac{G_{\text{zip}} v_q - i_{pq}}{T_i} \tag{28}$$

$$\dot{i_{qd}} = \frac{-B_{\text{zip}} v_q - i_{qd}}{T_i}, \quad \dot{i_{qq}} = \frac{B_{\text{zip}} v_d - i_{qq}}{T_i} \tag{29}$$

where T_i is the time constant of the load. The interface with the grid is done adding the total current of the ZIP load ($i_{\text{zip}} = i_p + i_q$) to the Kirchoff equations in each connection node.

D. IM Model

For the IM, the flux equations are

$$\psi_{s_{dq}} = L_s i_{s_{dq}} + L_m(i_{s_{dq}} + i_{r_{dq}}) \tag{30}$$
$$\psi_{r_{dq}} = L_r i_{r_{dq}} + L_m(i_{s_{dq}} + i_{r_{dq}}) \tag{31}$$

where subscripts s and r refer to the magnitudes of current i, induction L, and flux ψ of the stator and the rotor, respectively. L_m represents the magnetizing inductance. The voltage equations are

$$v_{s_{dq}} = r_s i_{s_{dq}} \mp \omega \psi_{s_{qd}} + \dot{\psi_{s_{dq}}} \tag{32}$$
$$v_{r_{dq}} = r_r i_{r_{dq}} \mp (\omega - \omega_r)\psi_{r_{qd}} + \dot{\psi_{r_{dq}}}. \tag{33}$$

By short circuiting the rotor and combining (30)–(33), the model for the IM is derived. Together with the electromechanical equation that defines the acceleration of the shaft of the motor $\dot{\omega_r}$, the complete model for the IM can be written as follows:

$$\dot{\omega_r} = \frac{p}{2J}(T_{el} - T_{\text{load}}) \tag{34}$$
$$\dot{\psi_{r_d}} = (\omega - \omega_r)\psi_{r_q} - r_r i_{r_d} \tag{35}$$
$$\dot{\psi_{r_q}} = -(\omega - \omega_r)\psi_{r_d} - r_r i_{r_q} \tag{36}$$
$$\dot{i_{s_d}} = \frac{1}{L_m + L_s - \frac{L_m^2}{L_r + L_m}}(v_{s_d} - r_s i_{s_d} + \omega \psi_{s_q} - \frac{L_m}{L_r + L_m}((\omega - \omega_r)\psi_{r_q} - r_r i_{r_d})) \tag{37}$$
$$\dot{i_{s_q}} = \frac{1}{L_m + L_s - \frac{L_m^2}{L_r + L_m}}(v_{s_q} - r_s i_{s_d} - \omega \psi_{s_d} + \frac{L_m}{L_r + L_m}((\omega - \omega_r)\psi_{r_d} + r_r i_{r_q})) \tag{38}$$

where J is the inertia constant. The electrical torque can be written as

$$T_{el} = \frac{3}{2}\frac{p}{2}(\psi_{r_q} i_{r_d} - \psi_{r_d} i_{r_q}) \tag{39}$$

where p is the pair of poles of the machine.

For the mechanical torque, a polynomial load is used

$$T_{\text{load}} = K_0 + K_1\omega + K_2\omega^2 \tag{40}$$

where K_0, K_1, and K_2 are parameters to model the load.

REFERENCES

[1] P. Kundur, N. Balu, and M. Lauby, *Power System Stability and Control* (EPRI Power System Engineering Series). New York, NY, USA: McGraw-Hill, 1994.

[2] J. P. Lopes, N. Hatziargyriou, J. Mutale, P. Djapic, and N. Jenkins, "Integrating distributed generation into electric power systems: A review of drivers, challenges and opportunities," *Electr. Power Syst. Res.*, vol. 77, no. 9, pp. 1189–1203, 2007.

[3] N. Hatziargyriou, *Microgrids: Architectures and Control*. Hoboken, NJ, USA: Wiley, 2014.

[4] J. A. P. Lopes, F. J. Soares, and P. M. R. Almeida, "Integration of electric vehicles in the electric power system," *Proc. IEEE*, vol. 99, no. 1, pp. 168–183, Jan. 2010.

[5] N. Pogaku, M. Prodanovic, and T. C. Green, "Modeling, analysis and testing of autonomous operation of an inverter-based microgrid," *IEEE Trans. Power Electron.*, vol. 22, no. 2, pp. 613–625, Mar. 2007.

[6] C. Canizares, *Voltage Stability Assessment: Concepts, Practices and Tools* (Special Publication of IEEE Power System Stability Subcommittee), C. Canizares, Ed. Piscataway, NJ, USA: IEEE Power Energy Soc., 2002.

[7] T. van Cutsem and C. Vournas, *Voltage Stability of Electric Power Systems*. New York, NY, USA: Springer, 2007.

[8] Y. A. Kuznetsov, *Elements of Applied Bifurcation Theory*, vol. 112. New York, NY, USA: Springer, 2013.

[9] S. H. Strogatz, *Nonlinear Dynamics and Chaos With Student Solutions Manual: With Applications to Physics, Biology, Chemistry, and Engineering*. Boca Raton, FL, USA: CRC Press, 2018.

[10] C. A. Canizares, "On bifurcations, voltage collapse and load modeling," *IEEE Trans. Power Syst.*, vol. 10, no. 1, pp. 512–522, Feb. 1995.

[11] I. Dobson and H.-D. Chiang, "Towards a theory of voltage collapse in electric power systems," *Syst. Control Lett.*, vol. 13, no. 3, pp. 253–262, 1989.

[12] V. Ajjarapu and B. Lee, "Bifurcation theory and its application to nonlinear dynamical phenomena in an electrical power system," *IEEE Trans. Power Syst.*, vol. 7, no. 1, pp. 424–431, Feb. 1992.

[13] H. Iu and C. Tse, "Bifurcation behavior in parallel-connected buck converters," *IEEE Trans. Circuits Syst. I, Fundam. Theory Appl.*, vol. 48, no. 2, pp. 233–240, Feb. 2001.

[14] S. Parui and S. Banerjee, "Bifurcations due to transition from continuous conduction mode to discontinuous conduction mode in the boost converter," *IEEE Trans. Circuits Syst. I: Fundam. Theory Appl.*, vol. 50, no. 11, pp. 1464–1469, Nov. 2003.

[15] C. Tse, Y. Lai, and H. Iu, "Hopf bifurcation and chaos in a free-running current-controlled Cuk switching regulator," *IEEE Trans. Circuits Syst. I: Fundam. Theory Appl.*, vol. 47, no. 4, pp. 448–457, Apr. 2000.

[16] C. Reza and D.-C. Lu, "Recent progress and future research direction of nonlinear dynamics and bifurcation analysis of grid-connected power converter circuits and systems," *IEEE Trans. Emerg. Sel. Topics Power Electron.*, vol. 8, no. 4, pp. 3193–3203, Dec. 2019.

[17] E. Lenz, D. J. Pagano, and J. Pou, "Bifurcation analysis of parallel-connected voltage-source inverters with constant power loads," *IEEE Trans. Smart Grid*, vol. 9, no. 6, pp. 5482–5493, Nov. 2018.

[18] A. P. N. Tahim, D. J. Pagano, E. Lenz, and V. Stramosk, "Modeling and stability analysis of islanded DC microgrids under droop control," *IEEE Trans. Power Electron.*, vol. 30, no. 8, pp. 4597–4607, Aug. 2015.

[19] E. Lenz, D. J. Pagano, A. Ruseler, and M. L. Heldwein, "Two-parameter stability analysis of resistive droop control applied to parallel-connected voltage-source inverters," *IEEE Trans. Emerg. Sel. Topics Power Electron.*, vol. 8, no. 4, pp. 3318–3332, Dec. 2020.

[20] G. Diaz, C. Gonzalez-Moran, J. Gomez-Aleixandre, and A. Diez, "Scheduling of droop coefficients for frequency and voltage regulation in isolated microgrids," *IEEE Trans. Power Syst.*, vol. 25, no. 1, pp. 489–496, Feb. 2010.

[21] Z. Shuai, Y. Hu, Y. Peng, C. Tu, and Z. J. Shen, "Dynamic stability analysis of synchronverter-dominated microgrid based on bifurcation theory," *IEEE Trans. Ind. Electron.*, vol. 64, no. 9, pp. 7467–7477, Sep. 2017.

[22] Z. Shuai, Y. Peng, X. Liu, Z. Li, J. M. Guerrero, and J. Shen, "Parameter stability region analysis of islanded microgrid based on bifurcation theory," *IEEE Trans. Smart Grid*, vol. 10, no. 6, pp. 6580–6591, Nov. 2019.

[23] G. Revel, A. E. Leon, D. M. Alonso, and J. L. Moiola, "Dynamics and stability analysis of a power system with a PMSG-based wind farm performing ancillary services," *IEEE Trans. Circuits Syst. I: Reg. Papers*, vol. 61, no. 7, pp. 2182–2193, Jul. 2014.

[24] G. Revel, A. E. Leon, D. M. Alonso, and J. L. Moiola, "Multi-parameter bifurcation analysis of subsynchronous interactions in DFIG-based wind farms," *Electr. Power Syst. Res.*, vol. 140, pp. 643–652, 2016.

[25] H. Zong *et al.*, "Analysis of bifurcation behaviors in MMC connected to a weak grid," in *Proc. 44th Annu. Conf. IEEE Ind. Electron. Soc.*, 2018, pp. 1687–1692.

[26] M. Huang, S.-C. Wong, K. T. Chi, and X. Ruan, "Catastrophic bifurcation in three-phase voltage-source converters," *IEEE Trans. Circuits Syst. I: Reg. Papers*, vol. 60, no. 4, pp. 1062–1071, Apr. 2013.

[27] M. Huang, Y. Peng, K. T. Chi, Y. Liu, J. Sun, and X. Zha, "Bifurcation and large-signal stability analysis of three-phase voltage source converter under grid voltage dips," *IEEE Trans. Power Electron.*, vol. 32, no. 11, pp. 8868–8879, Nov. 2017.

[28] D. Moutevelis, J. Roldán-Pérez, M. Prodanovic, and S. S. Acevedo, "Bifurcation analysis of converter-dominated electrical distribution systems," in *Proc. IEEE Energy Convers. Congr. Expo.*, 2020, pp. 1670–1677.

[29] P. Kundur, K. Morison, and B. Gao, "Practical considerations in voltage stability assessment," *Int. J. Elect. Power Energy Syst.*, vol. 15, no. 4, pp. 205–215, 1993.

[30] T. Zhu, S. Tso, and K. Lo, "An investigation into the OLTC effects on voltage collapse," *IEEE Trans. Power Syst.*, vol. 15, no. 2, pp. 515–521, May 2000.

[31] Q. Zhou and J. Bialek, "Generation curtailment to manage voltage constraints in distribution networks," *IET Gener., Transmiss. Distrib.*, vol. 1, no. 3, pp. 492–498, 2007.

[32] G. Valverde and T. van Cutsem, "Model predictive control of voltages in active distribution networks," *IEEE Trans. Smart Grid*, vol. 4, no. 4, pp. 2152–2161, Dec. 2013.

[33] L. Huang, H. Xin, Z. Wang, L. Zhang, K. Wu, and J. Hu, "Transient stability analysis and control design of droop-controlled voltage source converters considering current limitation," *IEEE Trans. Smart Grid*, vol. 10, no. 1, pp. 578–591, Jan. 2019.

[34] Y. Hu, Y. Peng, and Z. Shuai, "Bifurcation analysis of the islanded microgrid with constant power loads," *J. Eng.*, vol. 2017, no. 13, pp. 1912–1917, 2017.

[35] G. Xing, Y. Min, L. Chen, and H. Mao, "Limit induced bifurcation of grid-connected VSC caused by current limit," *IEEE Trans. Power Syst.*, vol. 36, no. 3, pp. 2717–2720, May 2021.

[36] A. S. Sedra and K. C. Smith, *Microelectronic Circuits*. New York, NY, USA: Oxford Univ. Press, 1998.

[37] K. Srivastava and S. Srivastava, "Application of Hopf bifurcation theory for determining critical value of a generator control or load parameter," *Int. J. Elect. Power Energy Syst.*, vol. 17, no. 5, pp. 347–354, 1995.

[38] A. Lerm, F. Lemos, A. e Silva, and M. Irving, "Voltage stability assessment with inclusion of hard limits," *Proc. Inst. Elect. Eng.—Gener., Transmiss. Distrib.*, vol. 145, no. 5, pp. 505–510, 1998.

[39] A. Dhooge, W. Govaerts, and Y. A. Kuznetsov, "MATCONT: A MATLAB package for numerical bifurcation analysis of ODEs," *ACM Trans. Math. Softw.*, vol. 29, no. 2, pp. 141–164, 2003.

[40] Y. Zhu and K. Tomsovic, "Adaptive power flow method for distribution systems with dispersed generation," *IEEE Trans. Power Del.*, vol. 17, no. 3, pp. 822–827, Jul. 2002.

[41] N. Mahmud and A. Zahedi, "Review of control strategies for voltage regulation of the smart distribution network with high penetration of renewable distributed generation," *Renewable Sustain. Energy Rev.*, vol. 64, pp. 582–595, 2016.

[42] A. Yazdani and R. Iravani, *Voltage-Sourced Converters in Power Systems*. Hoboken, NJ, USA: Wiley, 2010.

[43] V. I. Arnol'd, *Catastrophe Theory*. New York, NY, USA: Springer, 2003.

[44] R. J. Avalos, C. A. Canizares, F. Milano, and A. J. Conejo, "Equivalency of continuation and optimization methods to determine saddle-node and limit-induced bifurcations in power systems," *IEEE Trans. Circuits Syst. I, Reg. Papers*, vol. 56, no. 1, pp. 210–223, Jan. 2009.
[45] W. Gu, F. Milano, P. Jiang, and G. Tang, "Hopf bifurcations induced by SVC controllers: A didactic example," *Electr. Power Syst. Res.*, vol. 77, nos. 3/4, pp. 234–240, 2007.
[46] N. G. Sakellaridis, M. E. Karystianos, and C. D. Vournas, "Local and global bifurcations in a small power system," *Int. J. Elect. Power Energy Syst.*, vol. 33, no. 7, pp. 1336–1347, 2011.
[47] P. W. Sauer, M. A. Pai, and J. H. Chow, *Power System Dynamics and Stability: With Synchrophasor Measurement and Power System Toolbox*. Hoboken, NJ, USA: Wiley, 2017.
[48] W. D. Rosehart and C. A. Cañizares, "Elimination of algebraic constraints in power system studies," in *Proc. Conf. IEEE Can. Conf. Electr. Comput. Eng.*, 1998, vol. 2, pp. 685–688.
[49] M. Abramowitz and I. A. Stegun, *Handbook of Mathematical Functions with Formulas, Graphs, and Mathematical Tables*, vol. 55. Washington, DC, USA: U.S. Govt. Printing Office, 1970.
[50] K. J. Åström, T. Hägglund, and K. J. Astrom, *Advanced PID Control*, vol. 461. Research Triangle Park, NC, USA: Instrum., Syst., Autom. Soc., 2006.
[51] I. A. Hiskens, "Trajectory deadlock in power system models," in *Proc. IEEE Int. Symp. Circuits Syst.*, 2011, pp. 2721–2724.
[52] M. A. A. Murad and F. Milano, "Modeling and simulation of PI-controllers limiters for the dynamic analysis of VSC-based devices," *IEEE Trans. Power Syst.*, vol. 34, no. 5, pp. 3921–3930, Sep. 2019.
[53] K. Clark, N. W. Miller, and J. J. Sanchez-Gasca, "Modeling of GE wind turbine-generators for grid studies," GE Energy, Atlanta, GA, USA, Tech. Rep. 0885-8950, 2010, vol. 4.
[54] *IEEE Standard for Interconnection and Interoperability of Distributed Energy Resources With Associated Electric Power Systems Interfaces*, IEEE Standard 1547-2018 (Revision of IEEE Standard 1547-2003), 2018, pp. 1–138.
[55] M. S. El Moursi, W. Xiao, and J. L. Kirtley, Jr., "Fault ride through capability for grid interfacing large scale PV power plants," *IET Gener., Transmiss. Distrib.*, vol. 7, no. 9, pp. 1027–1036, 2013.
[56] A. Mullane, G. Lightbody, and R. Yacamini, "Wind-turbine fault ride-through enhancement," *IEEE Trans. Power Syst.*, vol. 20, no. 4, pp. 1929–1937, Nov. 2005.
[57] A. Ortega and F. Milano, "Generalized model of VSC-based energy storage systems for transient stability analysis," *IEEE Trans. Power Syst.*, vol. 31, no. 5, pp. 3369–3380, Sep. 2015.
[58] E. Acha and B. Kazemtabrizi, "A new STATCOM model for power flows using the Newton-Raphson method," *IEEE Trans. Power Syst.*, vol. 28, no. 3, pp. 2455–2465, Aug. 2013.
[59] T. Gonen, *Electrical Power Transmission System Engineering: Analysis and Design*. Boca Raton, FL, USA: CRC Press, 2011.
[60] P. C. Krause, O. Wasynczuk, S. D. Sudhoff, and S. Pekarek, *Analysis of Electric Machinery and Drive Systems*, vol. 2. Hoboken, NJ, USA: Wiley, 2002.
[61] G. Revel, A. E. Leon, D. M. Alonso, and J. L. Moiola, "Bifurcation analysis on a multimachine power system model," *IEEE Trans. Circuits Syst. I, Reg. Papers*, vol. 57, no. 4, pp. 937–949, Apr. 2010.
[62] M. Prodanovic, A. Rodríguez-Cabero, M. Jiménez-Carrizosa, and J. Roldán-Pérez, "A rapid prototyping environment for DC and AC microgrids: Smart Energy Integration Lab (SEIL)," in *Proc. IEEE 2nd Int. Conf. DC Microgrids*, 2017, pp. 421–427.
[63] F. Huerta, J. K. Gruber, M. Prodanovic, and P. Matatagui, "Power-hardware-in-the-loop test beds: Evaluation tools for grid integration of distributed energy resources," *IEEE Ind. Appl. Mag.*, vol. 22, no. 2, pp. 18–26, Mar./Apr. 2016.
[64] F. Huerta, D. Pizarro, S. Cobreces, F. J. Rodriguez, C. Giron, and A. Rodriguez, "LQG servo controller for the current control of LCL grid-connected voltage-source converters," *IEEE Trans. Ind. Electron.*, vol. 59, no. 11, pp. 4272–4284, Nov. 2012.

Dionysios Moutevelis received the M.Eng. degree in electrical and computer engineering from the National Technical University of Athens, Athens, Greece, in 2017.

In 2019, he joined IMDEA Energy Institute, Madrid, Spain, where he is currently a Predoctoral Researcher. His research interests include stability analysis of power systems and power converter control.

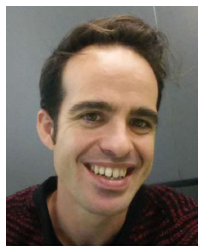

Javier Roldán-Pérez (Member, IEEE) received the B.S. degree in industrial engineering, the M.S. degree in electronics and control systems, the M.S. degree in system modeling, and the Ph.D. degree in power electronics all from Comillas Pontifical University, Madrid, Spain, in 2009, 2010, 2011, and 2015, respectively.

From 2010 to 2015, he was with the Institute for Research in Technology, Comillas University. In 2014, he was a visiting Ph.D. student with the Department of Energy Technology, Aalborg University, Aalborg, Denmark. From 2015 to 2016, he was with Electric and Control Systems Department, Norvento Energía Distribuida. In September 2016, he joined Electrical Systems Unit, IMDEA Energy Institute, Madrid. In 2018, he was a Researcher with SINTEF Energy Research, Trondheim, Norway. His research interests include the integration of renewable energies, microgrids, and power electronic applications.

Milan Prodanovic (Member, IEEE) received the B.Sc. degree in electrical engineering from the University of Belgrade, Belgrade, Serbia, in 1996, and the Ph.D. degree in electric and electronic engineering from Imperial College London, London, U.K., in 2004.

From 1997 to 1999, he was with GVS Engineering Company, Niš, Serbia, developing uninterruptible power supply systems. From 1999 to 2010, he was a Research Associate in electrical and electronic engineering with Imperial College London. He is currently a Senior Researcher and the Head of the Electrical Systems Unit, IMDEA Energy Institute, Madrid, Spain. He authored a number of highly cited articles and is the holder of three patents. His research interests include design and control of power electronics interfaces for distributed generation, microgrids stability and control, and active management of distribution networks.

Santiago Sanchez-Acevedo (Member, IEEE) received the bachelor's degree in electrical power engineering and the master's degree from the Universidad Tecnológica de Pereira, Pereira, Colombia, in 2006 and 2008, respectively, and the Ph.D. degree in electric power engineering from the Norwegian University of Science and Technology (NTNU), Trondheim, Norway, in 2015.

In 2016, he joined as a Postdoctoral Research Fellow with NTNU, where he was the main academic Researcher in the project CLUDGRID for interoperability of high-voltage dc transmission systems. Since 2019, he has been a Research Scientist with SINTEF Energy Research, Trondheim, where he is involved in projects regarding power system stability, HVdc transmission systems, laboratory analysis of digital substations, validation of cyber-physical power systems, and cyber-security.